NTNU – Trondheim
Norwegian University of
Science and Technology

A comparison of Gravity Wave Parameters derived from the Analysis of a Three-Field Photometer with Imagers

Irene Bakken

Master of Science in Physics and Mathematics
Submission date: June 2015
Supervisor: Patrick Joseph Espy, IFY

Norwegian University of Science and Technology
Department of Physics

Abstract

A method for preprocessing and analysing a few select fields in airglow intensity images from an all-sky imager was developed and utilized. Waves detected with a three-field analysis were compared with those waves visually detected in the images to evaluate the option of replacing or supplementing expensive imager systems with lower cost three-field photometers. The small-field analysis developed and utilized in this work yields accurate estimates of wave period, given data with a sufficienty high sampling frequency. The quality of wavelength and propagation direction estimates depends strongly on the field configuration, but overall, these wave parameters are estimated with less accuracy than the period. By comparison, event analyses are well suited for deriving the wavelength of short-period waves, but the periods are more uncertain. The method of analysis developed in this work demonstrates that the utilization of small-field observation systems like photometer-systems or telescopes, when optimized, has great potential to supplement and extend imager observations.

Sammendrag

En metode for forbehandling og analyse av et utvalg sirkulære felt i bilder av nattglødintensitet tatt med infrarødt kamera, ble utviklet og benyttet. Bølger identifisert med tre-felt-analysen ble sammenlignet med bølgene visuelt identifisert i bildene for å evaluere muligheten for å skifte ut eller supplementere dyre kamerasystemer med billigere tre-felt-fotometere. Analysen for små felt utviklet og benyttet i dette prosjektet ga nøyaktige bølgeperiodeestimater, så fremt dataene hadde høy nok samplingsfrekvens. Kvaliteten på estimatene av bølgelengde og bølgeforplantningsretningen avhenger mye av feltkonfigurasjonen, men alt i alt er disse bølgeparameterne estimert med lavere nøyaktighet enn perioden. Til sammenlikning er visuell analyse godt egnet for å bestemme bølgelengden av bølger med kort periode, men estimatet av periodene er mer usikre. Analysemetoden utviklet i dette prosjektet demonstrer at bruken av små-felt observasjonssystemer som fotometersystemer eller teleskoper kan, når den er optimalisert, ha et stort potensial i å supplementere og utvide kameraobservasjoner.

Preface

This thesis concludes my fifth and final year in the Physics and Mathematics M.Sc. program at the Norwegian University of Science and Technology in Trondheim. The work was carried out at the Department of Physics in the spring semester of 2015, as a continuation of my specialization project from the previous semester.

I'd like to thank my supervisor Prof. Patrick Joseph Espy for his guidance and weekly anecdotes, and Jacob Skauvold for proof-reading my thesis and providing dinner on late nights.

Trondheim, June 2015
Irene Bakken

Contents

List of Figures

List of Tables

1 Introduction

Atmospheric gravity waves are typically generated in the troposphere and propagate vertically and horizontally up through the atmosphere. As they pass through the Earth's airglow layers, they modulate the airglow intensity, which enables us to observe the horizontal components through the intensity variation. The airglow radiation is in the infrared part of the spectrum, and there are two main types of detectors to chose between; detectors with a field of view covering most/all of the sky (e.g. all-sky imager) and detectors covering one or several very small fields (e.g. three-field photometer).

The main objective of this work was to carry out a comparison of the two types of detectors, based on data from an all-sky imager. All-sky imagers and three-field photometers have been compared before (e.g. Reid and Woithe [2005]), but not simultaneously on the same night sky, or as in this case, on the exact same data. Nærø [2013] derived some horizontal wave parameters for waves detected in the all-sky images, and to complete the comparison, a method for deriving horizontal wave parameters from three (or more) small fields in the images was developed and utilized here.

The motivation for determining horizontal wave parameters is to estimate the flux of momentum carried into the mesosphere by atmospheric gravity waves. The waves grow in amplitude as they propagate upwards through a rapidly thinning atmosphere, until they become unstable and break, dissipating their energy and depositing their momentum to the surroundings [Andrews, 2010]. Determining the momentum flux carried by atmospheric gravity waves through the airglow layers, is the first step in estimating the momentum deposited in the upper atmosphere.

The momentum carried into the mesosphere by atmospheric gravity waves, greatly affects the winds and temperatures in the mesosphere/mesopause. Since atmospheric gravity waves are so important for the global circulation and thermal balance, they are a critical part of models of global cirulation, weather and climate. Due to the shortage of atmospheric gravity wave observations, we currently lack the knowledge of the seasonal and geographical behavior of wave-carried momentum flux needed to properly parametrize it's effect on the atmosphere [Espy et al., 2006].

An adequate analysis method for small-field observation systems would enable much simpler instruments to be used, and, possibly, enable detection of waves in astronomical background OH measurements, which there are extensive databases of. This would aid the community in acquiring

the atmospheric gravity wave observations needed to properly constrain the parametrizations used in models of the atmosphere. In the end, it is all done to further our understanding of the Earth's atmosphere and the beautiful, but fragile, ecosystem we live in.

2 Background

The Earth's atmosphere consists of a mixture of gases trapped within Earth's gravitational field, and interacts with land, ocean and space (mainly through photons and particles originating in the Sun). The following sections will describe the aspects of the atmosphere relevant to the observation of atmospheric gravity waves, and also introduce some methods for how to detect the waves.

2.1 Vertical Structure of the Atmosphere

The most common way of describing the vertical structure of the atmosphere is based on how the temperature varies with altitude. While pressure and density decrease nearly exponentially with altitude, temperature does not, since various reactions will heat or cool the atmosphere at different altitudes.

The five layers in this structure and their ranges are: the troposphere (0-15 km), the stratosphere (15-50 km), the mesosphere (50-85 or 50-90 km) and the thermosphere (85 or 90 km and upward) [Andrews, 2010]. The sign of the temperature gradient alternates between these layers; in the troposphere the temperature decreases with altitude, in the stratosphere it increases with altitude and so on. Figure 1 shows the temperature profile of the atmosphere and the names of the layers.

When observing atmospheric gravity waves, the upper mesosphere and lower thermosphere are of interest. This region is sometimes called the MLT-region (Mesosphere and Lower Thermosphere), and this is where we find the airglow layers.

2.2 Airglow Layers

The airglow layers are partially overlapping layers in the atmosphere that emit light in the visible and infrared parts of the electromagnetic spectrum. Various chemical and photochemical reactions result in the photo-

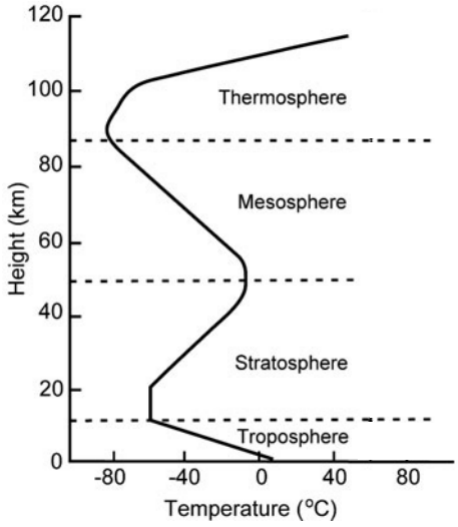

Figure 1: Vertical structure of the atmosphere based on the temperature gradient. Image source: http://www.azimuthproject.org/azimuth/show/Blog+-+the+color+of+night.

dissociation of many molecular species during the day. As these combine at night, excited molecular states are formed that relax through the emission of photons, producing the airglow. These emissions occur both at day and night, but at night the background radiation conditions are more favorable for observing the airglow from the ground.

The wavelength of the emitted light depends on the particles' initial and final states. Different layers are dominated by different particles, with different emission spectra. Sodium, oxygen (both atomic and molecular) are among the sources of the airglow [Woithe, 2000]. Due to it's high intensity, the hydroxyl (OH) airglow layer is commonly used in observations of gravity waves. Formed in by the recombination of atomic hydrogen with ozone in highly excited vibrational states, the emission layer has a vertical thickness of approximately 10 km and is situated at an altitude of about 87 km [Baker and Stair, 1988].

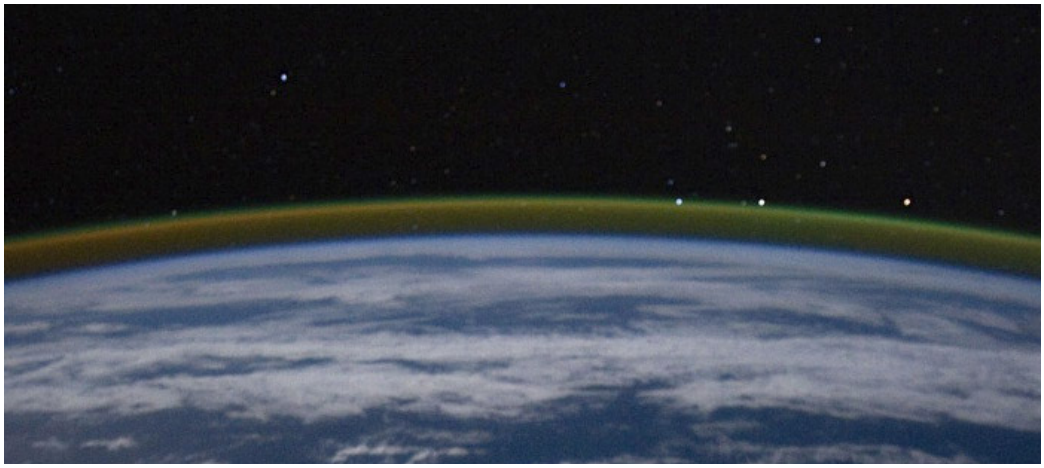

Figure 2: The airglow layers at the top of the Earth's atmosphere. Image credit: NASA.

2.3 Atmospheric Gravity Waves

A gravity wave is a mechanical wave whose restoring force is gravity/buoyancy. When a part of some fluid is vertically displaced in such a way that its surroundings are of lower density, gravity will pull it downwards. When it overshoots its equilibrium position it will be surrounded by fluids of higher density, and buoyancy will force it upwards again [Woithe, 2000]. For surface gravity waves this oscillation is constrained to some interface at a sharp density gradient. However, internal gravity waves may freely propagate through a three-dimensional density-stratified medium. Ocean waves with oscillating water droplets and atmospheric gravity waves with oscillating air parcels are examples of surface and internal gravity waves, respectively. From now on, atmospheric gravity waves will sometimes just be referred to as gravity waves.

2.3.1 Sources and propagation

Atmospheric gravity waves can be generated anywhere in the atmosphere, but those transporting energy from the troposphere and upwards are often the ones of interest. The most common gravity wave sources in the lower troposphere are topographic launching and various weather phenomena. Ex-

amples include wind blowing over mountains, frontal systems and thunderstorms. Other possible sources include some natural disasters; volcanic eruptions and earthquakes, sources of extraterrestrial origin; meteorites, auroral activity and solar-eclipses, and man-made sources; nuclear explosions and rocket launches. Some of the gravity waves observed may also be the remains of other waves [Nærø, 2013].

As the gravity waves propagate upwards through the atmosphere, through less and less dense air, the amplitude of the wave must increase for its energy to be conserved. Thus, the influence of gravity waves increases with altitude. When the wave becomes unstable and breaks, it deposits its momentum to the surroundings. At low altitudes, where the density is high, this momentum will not be able to move the air very far or fast. At high altitudes, where the density is low, the deposited momentum may greatly affect the movement of air in that region. Gravity waves collapsing in the mesosphere and thermosphere is what drives the global wind pattern known as the solstitial circulation, [Andrews, 2010] which is described in detail in the next section.

Not all gravity waves reach the mesosphere and the airglow layers. If a vertically-propagating gravity wave encounters a region of unstable atmosphere or background winds exceeding the phase velocity of the wave, it may break and deposit its momentum there [Medeiros et al., 2003, Nærø, 2013]. When observing gravity waves via emissions from airglow layers, only those waves which reach the layers will be detected, meaning only the energy deposited at this altitude or above may be calculated.

2.3.2 The Solstitial Circulation

The solstitial circulation is one of the reasons why we are interested in estimating the momentum carried by gravity waves up into the mesosphere. The mesosphere winds try to travel from the high-pressure at the summer pole to the low-pressure at the winter pole, but like all winds traveling from/toward a pole the Coriolis force turns them westward/eastward. However, due to a phenomenon known as wind filtering, atmospheric gravity waves will have a slight preference to a propagation direction in the opposite direction of the wind in the mesosphere. The momentum from breaking gravity waves gives a drag that results in a net force that will give the wind speed a component in the direction of the winter pole. This meridional circulation in the mesosphere is also called the solstitial circulation due to the fact the winds are

strongest in the winter and summer season [Andrews, 2010].

The solstitial circulation transports both energy and mass. In about three weeks a particle from the sunny summer pole can be transported down into the stratosphere above the dark winter pole. Since a number of chemical reactions depend on sunlight (mainly UV radiation), the solstitial circulation introduces 'out of season'-particles to the atmosphere above the winter pole. They may further affect the chemical composition of the atmosphere by reacting with other particles in that area. If, for example, nitrogen oxide (NO) is brought down into the stratosphere by the circulation, it will reduce the ozone (O_3) concentration, since NO is a catalyst to a reaction where O_3 is split into oxygen molecules (O_2) (P. Espy, personal communication, September, 2014).

2.3.3 Interaction with Airglow Layers

As an atmospheric gravity wave moves through the airglow layers, it will perturb the density and temperature of the layers. This affects the de-excitation process and thus the amount of emitted light. The correlation between the wave motion and the changes in the intensity of the emissions is what enables us to use the airglow layers to observe the horizontal components of gravity waves. The vertical wavelength needs to be, and usually is, much longer than the thickness of the layer ($\approx$ 10 km) [Nærø, 2013]. The gravity waves' horizontal components resemble plane, harmonic waves.

2.4 Detection of OH gravity waves

Methods for detecting atmospheric gravity waves include radar, lidar, satellite measurements and observations of airglow emissions [Nakamura et al., 1999]. The next two sections give a brief introduction to the all-sky imager and the three-(or more)-field photometer, which both measure airglow intensity. The main goal of this thesis is as mentioned to develop a method of analysing the data from the photometers and compare which waves were found to those observed by Nærø [2013] in all-sky imager data.

2.4.1 All-sky imager

The all-sky charged coupled device (CCD) imager is today the most common gravity wave detector. It is used to measure the intensity of one or more of

the bands in the spectrum emitted from the airglow layers. As the name suggests, this type of imager has a wide field of view. The imager at NTNU, Trondheim, which acquired the data considered in this work, has a 90° field of view.

It's wide field of view is is at once the all-sky imager's main advantage, and its main disadvantage. It gives a lot of information, but at the same time, the size of the CCD makes it expensive. An imager will easily cost 30-50k USD, software not included. Covering the whole sky also makes such imagers susceptible to saturation by moon light, light from aircraft or even cars and other objects on the ground. (P. Espy, personal communication, January 8, 2015).

There are two inherently different ways of analysing the airglow images from an all-sky imager. The oldest and still most frequently used, is event analysis, which is based on manual detection. The second method, spectral analysis, is fully automated.

There is more than one way of doing an event analysis, but they all entail identification of waves by visual inspection of captured airglow images. When a wave is found, wavelength can be determined from a still picture, period/phase speed and propagation direction from a series of images over time. The estimations may be done by a computer, but in the end it is the human that does the pattern recognition by marking the wave of interest.

Spectral analysis is a newer method than event analysis, and does not depend on humans for pattern recognition. A two- or three-dimensional discrete Fourier transform is applied to the image, reducing the time the analysis takes and the bias for waves easily spotted by the human eye [Matsuda et al., 2014]. Spectral analysis has it's own challenges of course, but the persisting popularity of event analysis appears to be caused as much by habit as by the performance of the method itself.

Both event analysis and spectral analysis require extensive preprocessing of images. Mapping to geographical coordinates, for example, is needed to compensate for the curvature of the depicted night sky; the pixels at the edges cover a larger area than in the middle. Another effect due to curvature of the sky, is that the thickness of the airglow layers along the line of sight will increase when moving away from zenith, meaning the intensity increase towards the edges of the image. Compensating for this effect is called flatfielding [Hatlen, 2013].

In order to utilize an event analysis, the background must be adequately removed so that the wave crests can be detected visually. One way of doing

this, which was utilized by Nærø [2013], is to subtract two images from each other. This also constitutes as flatfielding. An example of what this will look like is given in Figure 3. The light and dark stripes are a wave, the white dots are stars and the black dots next to them are where the stars were in the previous picture.

Figure 3: Difference image: the subtraction of two images of the OH airglow taken with an all-sky imager at Dragvoll, NTNU, Trondheim, November 18, 2012, at about 01:16.

2.4.2 Three-field photometer

A photometer does the same job as the imager, but has a much smaller field of view. A typical field of view would be about 1°, and this is the size used in examples from now on. In order to use photometers to detect gravity waves, at least three of them are needed. When referring to a three-field photometer, it is as a reminder that one field is not enough, but it may well

refer to an instrument with three or more small fields of view orientated on different part of the sky.

There are some advantages and disadvantages that come with the smaller fields of view. The photometers are for example less complex and cheaper than the all-sky imagers; the cost of a three-photometer system, with optics, is in the order of 15k EUR (17k USD). A single photometer with a movable mirror system to direct the beam at different angles i.e. at different fields in the sky, costs about the same (P. Espy, personal communication, June 9, 2015). Less preprocessing is needed for the data from the three-field photometer than an all-sky imager; the small field of view renders the curvature of the night sky negligible, and background removal is not as important when the analysis is done by a computer instead of a human. These advantages are traded in for less information, increasing the chance of misinterpreting the wavefield. One is also completely dependent on the computer analysis as it is not always possible to go back and visually identify the waves.

Using three or more photometers to do simultaneous sampling is not the only method that this work is relevant for. One may use a single photometer/telescope to move between the fields, as investigated in the author's specialization project, but one should beware of how the sampling frequency rapidly decreases with the number of fields. Another method would be to select a few fields (Section 3.1.5) in all-sky images and analyse them, exactly as is done in this work.

3 Method

The all-sky images were analysed using MATLAB. The following sections describe the steps taken to derive the waves' period, wavelength, propagation direction and time of observation from the images by studying three (or more) 1°-fields of the images.

3.1 Preprocessing

Before actually analysing the data, some preprocessing will reduce the chances of detecting waves where there are none. These steps don't depend on the actual data, but things like the sun's elevation, amount of cloud cover and the pixels per degree in the images. There are several ways of solving the problems presented in the following sections, but only the ones utilized in

this work will be described.

3.1.1 Discard data contaminated by sunlight

If the intensity measurements are taken while the sun is up, the sunlight will drown out any contribution from the airglow layers. The intensity as a function of time at one pixel in the images might look like the example in Figure 4; a broad, flat U. The sunlight will completely dominate the plot, and to avoid it being misinterpreted as a gravity wave, measurements affected by sunlight should be discarded.

To estimate sunset and sunrise at the height of the OH layer, the MATLAB function `SolarAzEl`, programmed by Koblick [2009], was used to determine when the solar depression angle (angle below horizon) at the ground reached 12° or more. As a rough estimate the shadow height in kilometers above the ground is equal to the square of the solar depression angle. In this case, the shadow height would be approximately 144 km, which is more than sufficient to cover the OH airglow layer. (P. Espy, personal communication, February 11, 2015). The solar depression angle depends on your location, so latitude, longitude and altitude are required input. In this case, the data were acquired at NTNU Campus Dragvoll, at N 63.41° E 10.47° and an altitude of approximately 0.15 km.

3.1.2 Discard data contaminated by clouds

Clouds reflect enough ground light in the infrared that some of it will register erroneously as OH airglow. The result is that clouds coming and going could be misinterpreted as gravity waves. In order to avoid this, data contaminated by clouds should be discarded. (P. Espy, personal communication, June 8, 2015). Figure 5 show an example of the measurements at one pixel contaminated by clouds (from about 22:00 and out).

Note that the analysis of the data depends on an approximately constant sampling period, meaning a data set with cloud contamination in the middle should be split in two and analysed separately. Data from an Andor spectrometer [NTNU] were used to determine when the cloud cover was detrimental to the OH intensity measurements by examining the strength of the IR sodium emissions emitted by street lamps that is reflected from the clouds [Hennum, 2013].

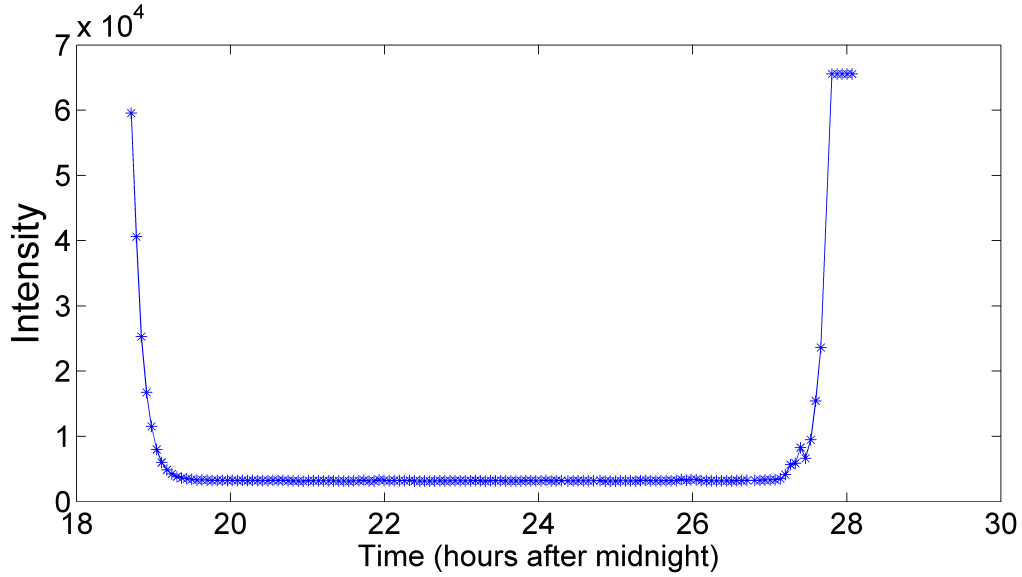

(a) Sunset and sunrise included.

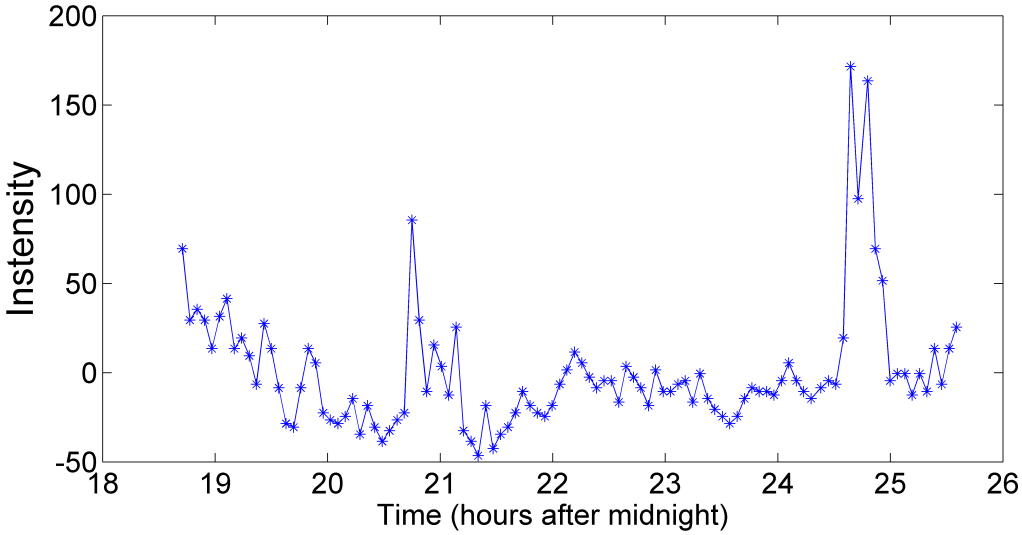

(b) Sunset and sunrise removed.

Figure 4: OH airglow intensity measurements acquired at Dragvoll, NTNU, Trondheim, March 30-31, 2013. The data is from one pixel in the images and (a) shows how the sunlight drowns out the variations in the intensity between sunset and sunrise, which are shown in (b).

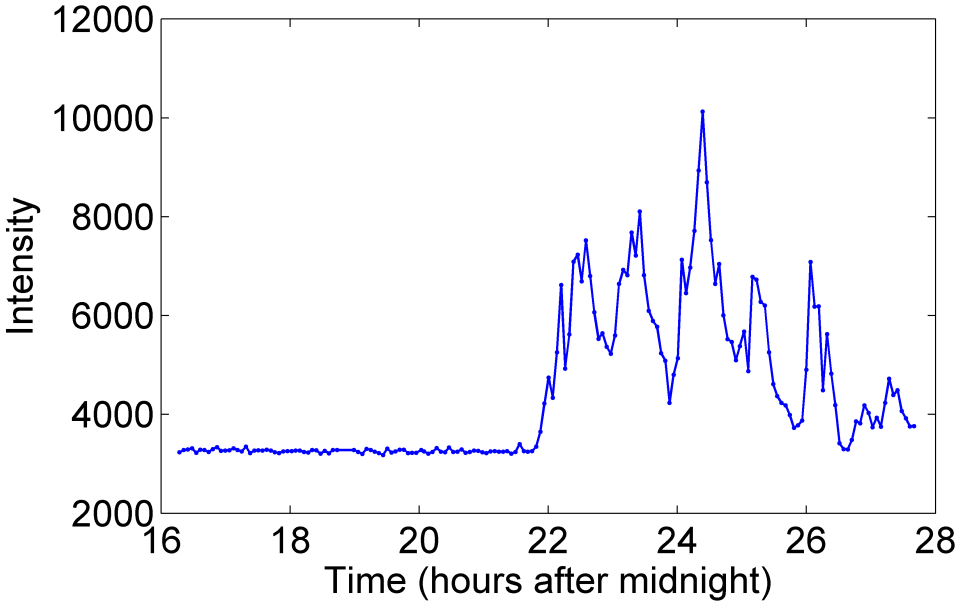

Figure 5: OH airglow intensity measurements acquired at Dragvoll, NTNU, Trondheim, December 6-7, 2012. The data is taken from one pixel in the images. From about 22:00 and until dawn, the measured radiation is mainly coming from clouds. The variation in intensity due to clouds is much larger than that due to OH airglow.

3.1.3 Locating zenith and the polar star

In order to derive an estimate for the propagation direction, one needs a reference system. The simplest way to obtain this, is by determining which direction is north, e.g. by locating zenith and the polar star. Zenith is not generally located in the excact center of the image, necessitating identification by other means. Locating zenith and the polar star can be done as part of the mapping to geographical coordinates. This usually involves comparing a star map to the position of the stars in the image. Mapping primarily compensates for the curvature of the sky and was considered unnecessary for an analysis of small fields close to zenith. Hatlen [2013] determined the locations of zenith and the polar star in the same images considered here. Hence, the current work makes use of the same locations.

3.1.4 Remove stars, hot pixels and background noise

Stars will show up on the all-sky images of the OH airglow as bright spots of varying sizes. Their intensity is much greater than both the background radiation and the wave crests due to gravity waves propagating through the airglow layers. Since the stars will move noticeable from image to image, they cannot be removed by simply subtracting two subsequent images. Complete star removal is a quite complex problem, so in this work a partially removal/dimming of the stars will be sufficient. The method used is a median filter which replaces each pixel in the image with the median intensity of the pixels in the neighborhood. The size of the neighborhood window should be chosen as large enough to remove most of the stars, while not being too large, as this would cause excessive blurring of the image. The normal pixel size of a star, and therefore also the best window size, will depend on number of pixels per degree in the image. Two examples of window choices were found; Matsuda et al. [2014] used a window of 21×21 pixels and Suzuki et al. [2007] used a window of 20×20 pixels.

In this work, window sizes of 2-30 were tested. For most of the data, little change was seen, while the running time escalated quickly. In the end a window of 10×10 pixels was chosen as a compromise with time efficiency on one side and effectiveness of star removal on the other. Figure 6 shows the effect a 10×10 median filter has on a data set containing a star; the spike due to the star is severely reduced, but so are the details in the data set. For each image the data are integrated over one field of 1°-field of view, as described in Section 3.1.5. Since the instrument used gives images with about 14 pixels per degree, the chosen window of the median filter is about the same size as the fields the data are integrated over, which seems like a reasonable choice. In order to reduce the spike from the star to normal noise level, a window of 25×25 was needed, which was very time consuming, but more in agreement with the choices made by Matsuda et al. [2014] and Suzuki et al. [2007] - assuming the pixel sizes of the stars are comparable.

Hot pixels and other so-called 'salt and pepper' noise will automatically be removed by the median filter.

There will be some background noise covering larger areas than stars and hot pixels, e.g. from the Milky Way. Most of the background noise is effectively removed by image subtraction, since it's the variation from image to image that is evaluated.

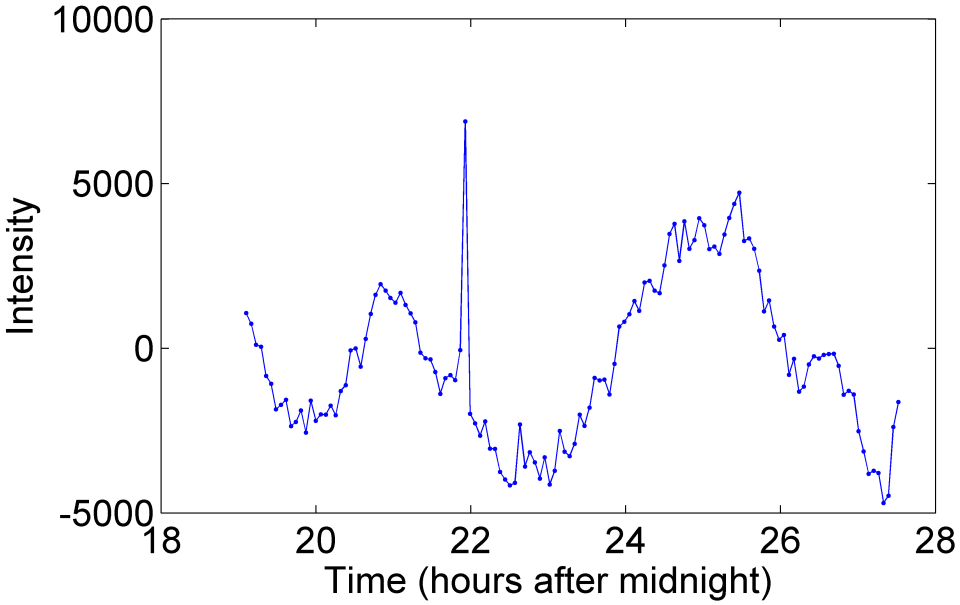

(a) No median filter.

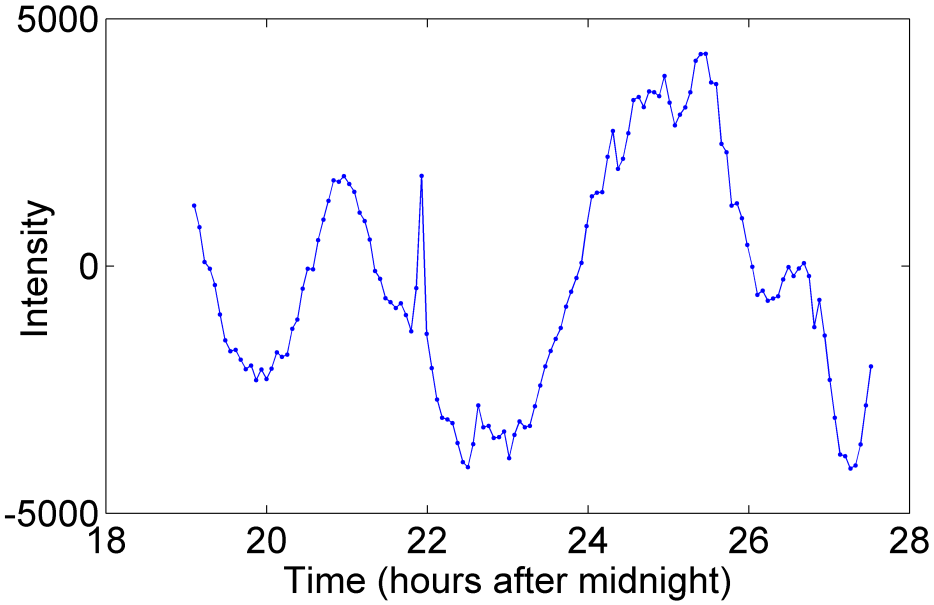

(b) A 10x10 median filter used.

Figure 6: OH airglow intensity measurements acquired at Dragvoll, NTNU, Trondheim, February 9-10, 2013. The data is taken from one 1°-field of the images, and the spike at about 22:00 is most likely due to a star. The data in (a) have not been filtered, while the data in (b) has been filtered with a 10x10 median filter.

3.1.5 Integrate data over chosen fields

The main idea of the method tested in this work, is that only three small fields of the images are actually necessary for deriving wave parameters. The number, placement and size of the fields are of course determined by the instrument and/or method utilized. Here, three circular fields of 1° each, all placed 3 km from zenith, were used.

The pixels within the given fields are located, and the intensity is integrated over each field i.e. the value of all the pixels within the field are summed. The result is one data series per field, describing intensity as a function of time. Since only variation in intensity is of interest, and not the actual intensity values, the mean is subtracted from each data series.

3.2 Analysis

When trying to untangle the waves in the wavefield from each other and determine their frequency and phase, it soon became clear that simply using MATLAB's built-in `fft` function did not, in itself, provide an adequate means of identifying individual waves. As one can see in Figure 7 there are small-amplitude waves superimposed on the larger ones (e.g. from 17:00 to 24:00). Additionally some waves are short-lived (e.g. from 02:20 to 03:20), and some have both small amplitudes and short durations. The `fft` function looks for waves that oscillate around zero and last for the whole data set, so these kinds of waves will be overlooked. The two next sections will describe the techniques used to counteract these problems. Repeated use of moving subtraction filters will enable us to search for both low and high frequency waves. The use of the wavelet transform will give suggested time intervals in which to look for waves. For each time interval one will determine the frequency of the waves and the time it takes for them to travel between the fields (Section 3.2.3). Then these wave parameters will be used to estimate the wavelength and propagation direction (Section 3.2.4).

3.2.1 The moving average subtraction filter

The moving average subtraction filter, from now on referred to as the MAS filter, is used to separate waves of different amplitudes. For each sample, it calculates the mean of the samples within a window of a chosen length L, centered on the sample of interest. Then the mean is subtracted from

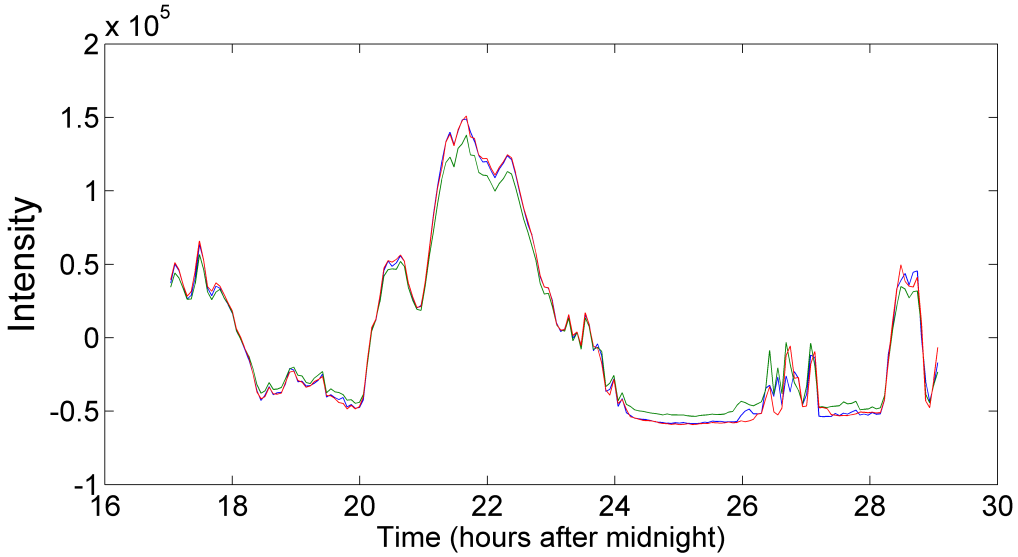

Figure 7: OH airglow intensity measurements acquired at Dragvoll, NTNU, Trondheim, November 17-18, 2012. The data has been preprocessed and is ready for analysis. The three different data sets are from integrating the intensity over three different fields. There seems to be some waves of smaller amplitude and period superimposed on larger ones (e.g. from 17:00 to 24:00) and very short waves not lasting the whole observation period (e.g. from 02:20 to 03:20).

the sample. The MAS filter is a high pass filter. The relation between the Fourier transforms of data sets X and Y, where Y is the result of using a MAS filter on X, is

$$F_Y(f) = F_X(f) \cdot H(f)$$

where $H(f)$ is the filter response for frequency f (in units of Hz)

$$H(f) = 1 - \frac{\sin(\pi L f / f_s)}{L \cdot \sin(\pi f / f_s)} \tag{1}$$

when the sampling frequency is f_s (in Hz) and the window length of the filter is L (dimensionless) [Kennedy, 1980]. An example of a MAS filter's effect on the power spectrum from a Fourier transform, $|H(f)|^2$, is shown in Figure 8 for a filter with $L = 25$ when the sampling frequency is $Fs = 100$. The cut-off frequency is at about $f_c \approx 0.76 \cdot f_s/L$, where 0.76 was determined empirically.

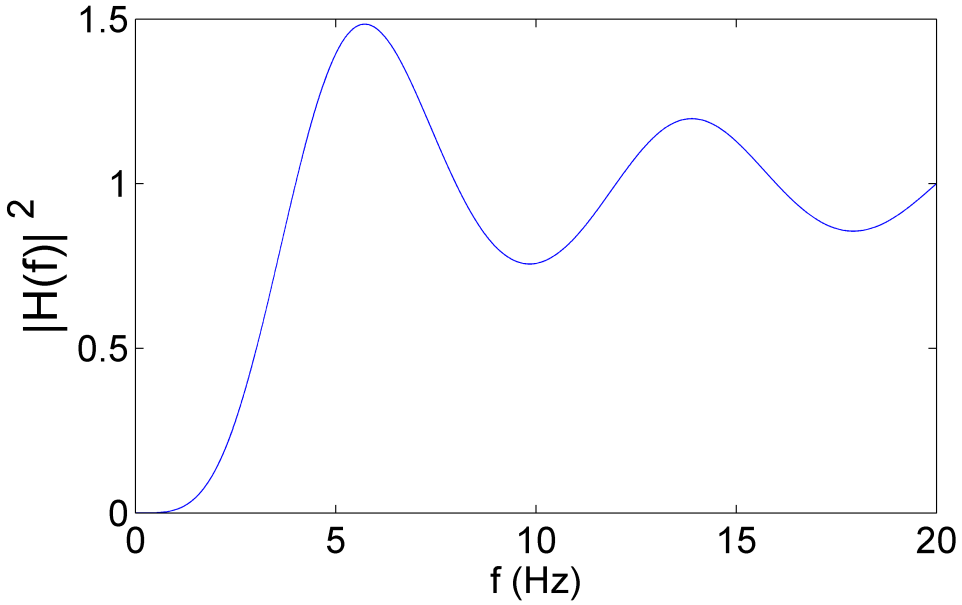

Figure 8: The plot shows the effect a MAS filter has on the power spectrum acquired by Fourier transform.

The effect the MAS filter has on the data set is shown in Figure 9. The first cut-off frequency is set to $f_c = 1/(\text{observation time})$ since at least two periods of the wave should be observed to determine it's existence. After the rest of the analysis has been performed on the filtered data set, a new cut-off frequency is determined based on the findings, and the data are filtered again to look for yet larger frequencies. In order to fulfill the Nyquist requirement, one must have $f_c/f_s < 0.5$, but a more strict requirement is recommended. Here the default requirement is $f_c/f_s < 1/4$.

3.2.2 The wavelet transform

In order to find short waves that don't last the whole observation period, a one dimensional wavelet transform, using the Morlet wavelet, was applied to the data. The wavelet software was provided by C. Torrence and G. Compo, and is (or was) available on the internet [Torrence and Compo]. Their program gives (among other things) a time-period diagram with information about the significance. An example is shown in Figure 10, where one can

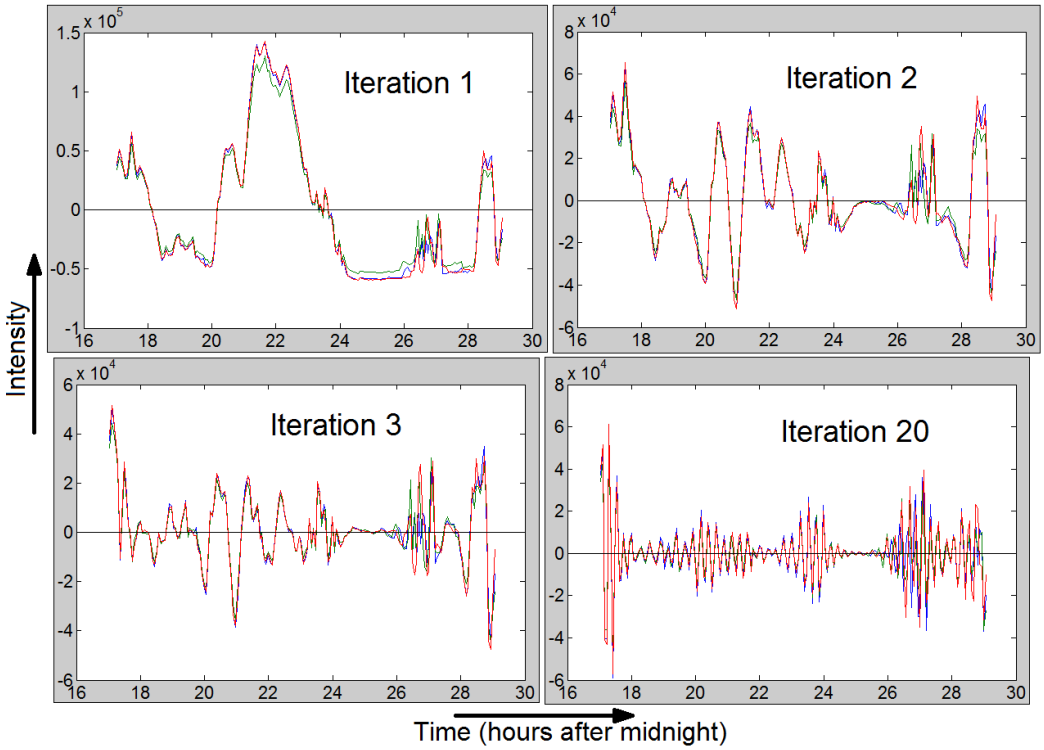

Figure 9: OH airglow intensity measurements acquired at Dragvoll, NTNU, Trondheim, November 17-18, 2012. The plots are from different iterations in the analysis procedure, where for each iteration a moving average subtraction filter of increasingly higher cut-off frequency has been applied. The plots are from the first (upper left), second (upper right), third (lower left) and twentieth (lower right) iteration. The twentieth iteration was also the last, since the estimated frequencies were getting too close to the Nyquist frequency to be reliable.

see which periods are significant at which times, and which periods at which times that will be affected by boundary effects [Torrence and Compo, 1998]. The matrix containing the information for the diagram was used to determine when a wave started and ended. The estimated periods and their significance were only used to tell waves apart. The wavelet transform gives no information about the phase of the wave, so using MATLAB's `fft` function is still necessary (Section 3.2.3).

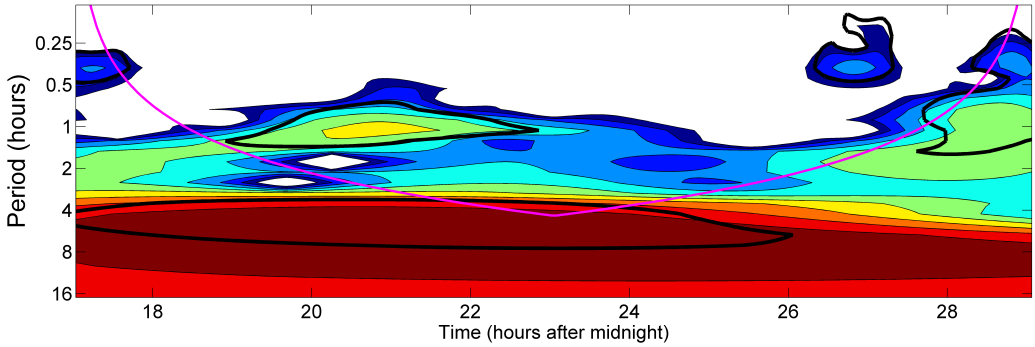

Figure 10: The period-time diagram returned by the wavelet transform. The black lines mark the areas with more than 95% significance, and the purple line marks the cone of interest (COI); below it the estimate of the period will experience boundary effects.

3.2.3 Determine frequency and travel time

From the wavelet transform, one has found time intervals of interest that should contain waves. Data from each time interval is henceforth analysed on it's own. The mean is subtracted again and a MAS filter removes all variations with periods longer than the time interval. A Hanning window is applied before MATLAB's `fft` function is used. The Fourier transform gives a frequency spectrum and phase spectrum for each field. Since the waves should move through all the fields with the same frequency, the power spectra are found from the frequency spectra and added to each other. Note that it is important to keep the information about the phase for all the fields. The power spectrum is also corrected for the known effect of the MAS filter for frequencies above the cut-off frequency. This should compensate for the amplification of frequencies just above the cut-off frequency, which after some iterations will result in noise appearing as high-frequency waves, as seen after the last and twentieth iteration in Figure 9.

The power spectrum is used to determine the frequency of the wave(s) in the time interval. A peak is found if it is greater than twice the standard deviation of the subset, 2σ, and the full width at half maximum (FWHM) is calculated. Since it is likely that a wave will be detected multiple times, mainly due to the iteration needed in order to use the MAS filter on the whole data set for increasingly higher cut-off frequencies, a way of determining the best estimate of the frequency and phase is needed. If two waves

in overlapping time intervals have equal (or close to) frequencies, they are considered to be the same wave. The estimate with the smallest FWHM is considered most accurate, and this frequency and (more importantly) phase is kept, while the others are discarded. Waves with frequencies so low compared to the length of the time interval that there is less than two periods of the wave to analyse, are discarded. Similarly, waves with frequencies so high that there is less than a required number of samples per wave period, are discarded. As mentioned above, the standard requirement used here is $f_c/f_s < 1/4$.

The wave will be in different phases when passing through the fields, and the phase differences are translated into the time the wave uses to travel between the fields. Depending on which direction the wave traveled, there will be two alternatives, but we assume that the fields are always hit in that order which minimizes the time difference. This is a good assumption as long as the distances between fields are small relative to the wavelength.

3.2.4 Determine wavelength and propagation direction

This section describes how wavelength and propagation direction can be determined from the frequency and travel time found in the previous section. The method was originally developed for the author's specialization project in fall 2014, and only the general idea of the method is given here.

Intensity measurements from at least three fields are needed for this method to work. Figure 11 illustrates how the travel time is connected to the distance between two of the fields and the orientation of the vector between the fields compared to the propagation direction of the wave. As one can see from the figure, the travel time Δt may be expressed as

$$\Delta t = \frac{d \cdot \cos(\alpha - \phi)}{c} = \frac{d \cdot \cos(\phi - \alpha)}{c} \tag{2}$$

where Δt is the travel time, d is the distance between the fields, ϕ is the propagation direction of the wave and α is the angle the vector between the fields makes with the z-axis of the chosen coordinate system. The phase speed of the wave, c, is unknown, but cancels if we take the ratio of the travel time of two pairs of fields. From Equation (2) the following expression for ϕ may be derived

$$\tan\phi = \frac{(\Delta t_B d_A)/(\Delta t_A d_B)\cos\alpha_A - \cos\alpha_B}{\sin\alpha_B - (\Delta t_B d_A)/(\Delta t_A d_B)\sin\alpha_A} \tag{3}$$

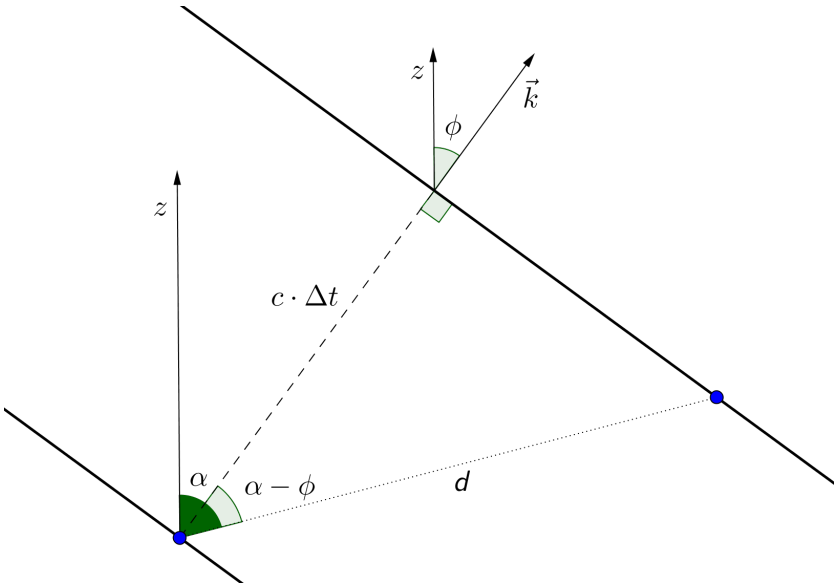

Figure 11: The geometry of the problem. The thick diagonal lines are parallel to the wave front, the k-vector is the wave vector and shows the propagation direction of the wave, which makes the angle ϕ with the z-axis. The wave is detected as it moves through the two (blue) fields which are a distance d apart, and Δt is the time it takes to travel between the fields. This makes $c \cdot \Delta t$ the true distance traveled by the wave between the fields, c being the phase speed of the wave. The orientation of the field pair is described by the angle the dotted line between them makes with the z-axis, α.

where the parameters marked A belong to one field pair, and those marked B belong to another pair. The order in which the wavefront hit the fields can be found from the sign of the travel time and is kept track of. Field pairs that encounter the same wavefront simultaneously ($\Delta t = 0$) must not be used in Equation (3). But, in such cases, the wave's propagation direction must be orthogonal to the vector between the fields, the only thing then needed to calculate ϕ is the placement of another field and knowing whether the wavefront hit it first. We also avoid comparing parallel pairs of fields and check which quadrant ϕ ended up in by comparing it to the order in which the wave hit the fields. When ϕ has been calculated, the wavelength λ can be determined with the following equation

$$\lambda_{obs} = \frac{c}{f} = \frac{d \cdot |\cos(\phi - \alpha)|}{\Delta t \cdot f}. \tag{4}$$

An estimate of the wavelength and propagation direction can be made for every pair of fields. So for e.g. three fields, one gets three estimates, while for four fields, one can get six. Small errors in the phase estimate can lead to great errors in wavelength and propagation direction, so outliers are looked for and removed. Note that finding integer multiples of the wavelength is common.

4 Results

The following sections present the results from the tests performed to enable a comparison between the analysis performed on the all-sky images by Nærø [2013] and the analysis method described in Section 3 performed on a few select fields in the same images. The characteristics of the last method were also investigated.

4.1 All waves detected with standard settings

The preprocessing and analysis method described in Section 3 was applied to all images corresponding to dates for which Nærø [2013] reported wave events. A configuration of three 1-° fields all 3 km from zenith, was used, and the sampling period was about 4 min. The upper bound to the ratio between the frequency of the waves and the sampling frequency was set to $f/f_s < 1/4$. A total of 36 wave events were detected, and the distributions of the estimated periods, observation times, wavelengths, phase speeds (wavelength divided by period) and propagation directions are presented in Figure 12.

4.2 Detection of the imager waves

The waves observed by Nærø [2013] are given in Table 1, along with their derived periods and wavelengths. The smallest wave frequency to sampling frequency ratio among Nærø's waves, corresponding to the largest period (770 s), is

$$f/f_s = T_s/T = 4 \cdot 60\text{s}/770\text{s} = 0.31$$

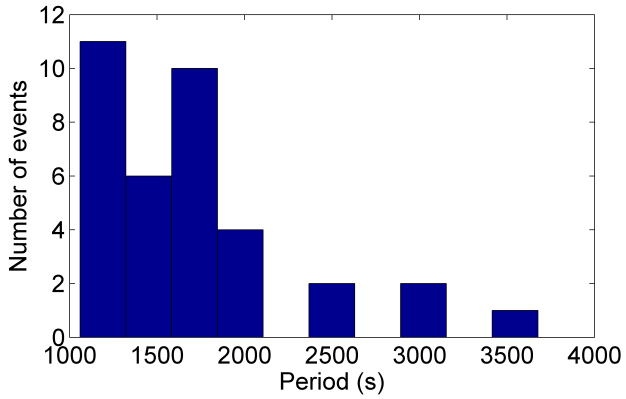

(a) Distribution of period estimates.

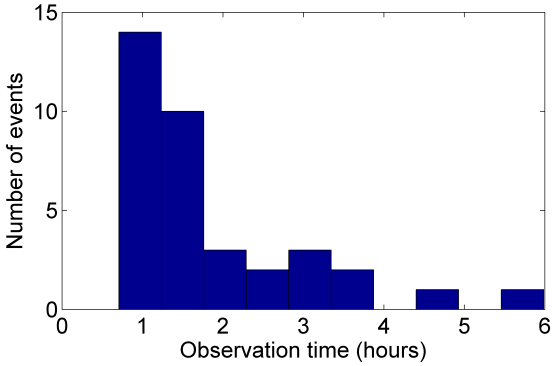

(b) Distribution of observation time.

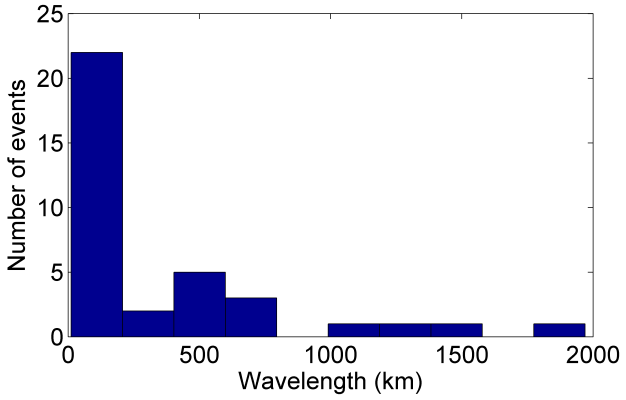

(c) Distribution of wavelength estimates.

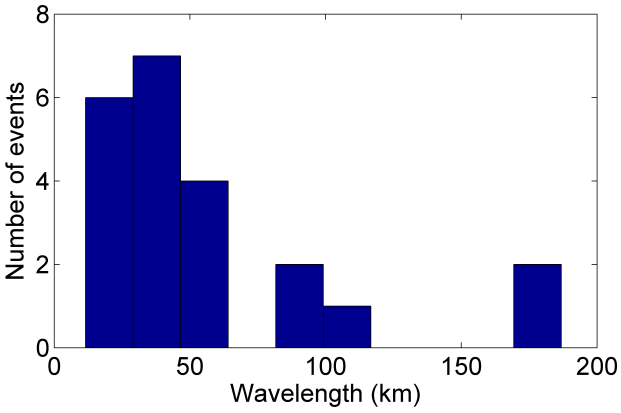

(d) Detail from distribution of wavelength estimates.

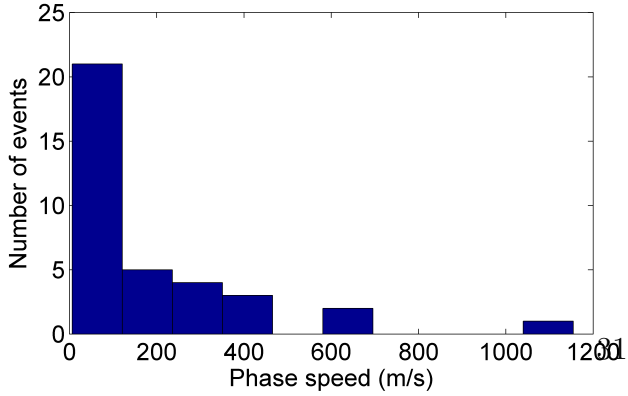

(e) Distribution of phase speed estimates.

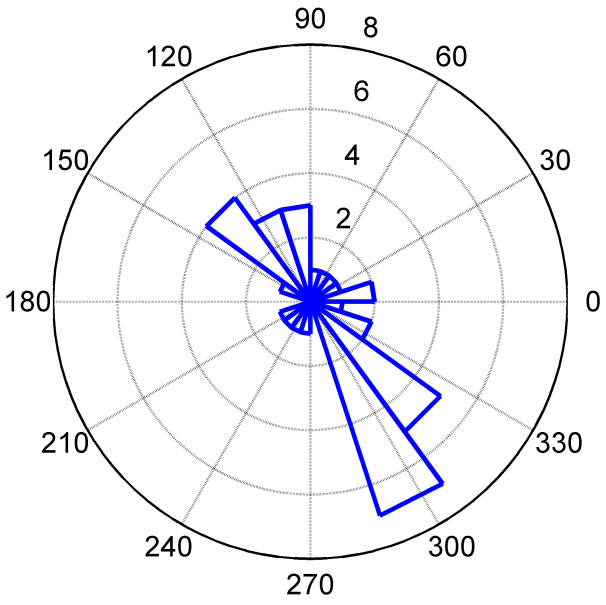

(f) Distribution of propagation direction estimates.

Figure 12: Wave parameters derived with standard settings in the analysis described in Section 3.2. In total, 36 wave events were detected.

which is larger than the set upper bound of 1/4. With this requirement, it is impossible to detect any of the waves Nærø observed.

Since Nærø's waves are our only basis for comparison, and only way of determining whether the method is applicable to real data, the upper bound to the ratio between frequency of the waves and the sampling frequency, was relaxed. It was set to $f/f_s < 0.49$, which allows virtually all waves that fulfill the Nyquist requirement. Two of Nærø's waves don't fulfill this criterion (Dec 3 and Feb 8), and will therefore be ignored.

The analysis from Section 3.2 was again applied, with a relaxed upper bound on the frequency, to the images from dates when Nærø observed waves. Among the waves that matched the time of night when Nærø observed a wave, the wave with the period estimate closest to Nærø's period, was assumed to possibly be the same wave as the Nærø wave. The estimated periods and wavelengths for these waves are given in Table 2 together with the relative difference between period- and wavelength estimates from [Nærø, 2013] and the current work.

Table 1: The date and time at which Nærø [2013] observed waves in images acquired at Dragvoll, NTNU, Trondheim, and the waves' period (in seconds), T_N, and wavelength (in kilometers), λ_N, derived by event analysis.

Date	*Time* (UTC)	T_N (s)	λ_N (km)
November 18, 2012	01:00	660	22.0
December 3, 2012	18:00	440	22.5
December 6, 2012	18-19	650	25.0
January 16, 2013	01:00	540	20.5
January 16, 2013	19:00	620	29.0
January 17, 2013	02:00	750	28.0
February 7, 2013	23:30	630	20.0
February 8, 2013	05:00	420	18.0
February 9, 2013	22:00	770	29.0
February 9, 2013	23:00	590	20.0
March 30, 2013	19:30	630	61.5

Table 2: The date and time at which Nærø [2013] observed waves in images acquired at Dragvoll, NTNU, Trondheim, that fulfill the Nyquist criterion. T and λ are the waves' period (in seconds) and wavelength (in kilometers), respectively, derived by the analysis method described in Section 3.2. $\Delta T/T_N$ is the relative difference between the period derived by the author and by Nærø [2013]; $(T - T_N)/T_N$. Equivalently, $\Delta\lambda/\lambda_N$ is the relative difference for the wavelength. The symbol — means no wave was detected at that time of night.

Date	*Time* (UTC)	T (s)	$\Delta T/T_N$	λ (km)	$\Delta\lambda/\lambda_N$
November 18, 2012	01:00	—	—	—	—
December 6, 2012	18-19	—	—	—	—
January 16, 2013	01:00	508	-6 %	88	327 %
January 16, 2013	19:00	556	-10 %	9	-69 %
January 17, 2013	02:00	834	11 %	11	-62 %
February 7, 2013	23:30	545	-14 %	11	-45 %
February 9, 2013	22:00	632	-18 %	8	-73 %
February 9, 2013	23:00	—	—	—	—
March 30, 2013	19:30	—	—	—	—

4.3 Simulation

In order to investigate some properties of the analysis method from Section 3.2, a short simulation study was performed, whereby the analysis was tested on synthetic data. The data were simulating a wave with a period of 750 seconds, a wavelength of 28 km and a propagation direction orthogonal to the line joining two of the three observation fields ($\phi = 300°$).

4.3.1 Simple wavefield

To investigate the effect of the complexity of the wavefield on the wave parameter estimates, a simulated wave ($T = 750$ s, $\lambda = 28$ km, $\phi = 300°$) was generated by sampling every 4 minutes, as before ($f_s = 1/(4 \text{ min}) \approx 0.00417$ Hz). The results are given in Table 3. The estimate of the period was better than for the corresponding wave in the complex wavefield, i.e. the 'January 17'-wave from Table 1. The estimate of the wavelength was essentially unchanged.

4.3.2 Increased sampling frequency

To investigate the effect of increasing the sampling frequency, a simulated wave ($T = 750$ s, $\lambda = 28$ km, $\phi = 300°$) was generated with a higher sampling frequency than used before; $f_s = 1/(1 \text{ min}) \approx 0.01667$ Hz. This gives a wave frequency to sampling frequency ratio well below the preferred upper bound of 1/4; $f/f_s = 60$ s/750 s= 0.08. Again, the results are given in Table 3. With these data, the estimate of the period was better than for the same wave, sampled at a quarter of the new sampling frequency. Again, the estimates of the wavelength and propagation direction were essentially unchanged.

4.3.3 Different field configurations

There are numerous and diverse field configurations to choose between. The one used earlier (three points, each 3 km from zenith) was chosen based on the author's experiences from the specialization project which this thesis is a continuation of. The parameters with the greatest effect on the quality of wave estimates are field separation and the number of fields, but certain propagation directions (those orthogonal to a line joining two fields) result in better estimates than others.

To investigate the effect of smaller field separation, all the distances were halved. The new fields were all situated 1.5 km from zenith, with 3 km as the greatest distance between them. A simulated wave ($T = 750$ s, $\lambda = 28$ km, $\phi = 300°$) was generated by sampling every 4 minutes, as usual, and integrated over the three new fields. The wave parameter estimates and their relative errors are given in Table 3. The estimate of the period is unchanged compared to the same wave sampled at the old fields. The estimate of the wavelength is greatly improved, while the estimated propagation direction appears to be off by 90°.

The same procedure was repeated for the same wave sampled every minute, sent through the new fields. The results are given in Table 3. Estimates of period, wavelength and propagation direction are greatly improved.

To investigate how the propagation direction effects the estimates, two new waves were simulated. The period and wavelength were unchanged ($T = 750$ s, $\lambda = 28$ km), but the propagation direction was changed by 20°, to $\phi = 320°$, for both of them. This ensures that the propagation direction is non-orthogonal to all lines between the fields. Both waves were sampled

every 4 minutes, but one was sent through the original field configuration (zenith-field distance: 3 km) and the other through the new one (zenith-field distance: 1.5 km). The results are given in Table 3. The period estimate is the same as it always is with a 4 min sampling period, whereas the estimates of the wavelength and propagation direction are worse than ever.

Table 3: Results from simulated waves passing through three fields with zenith-field distance d_{Z-F}, sampled every T_s seconds. The period was set to 750 seconds and the wavelength to 28 km, while the propagation direction (relative to north) was ϕ. T_e is the estimated period, λ_e is the estimated wavelength, ϕ_e is the estimated propagation direction, and $\Delta T/T$, $\Delta\lambda/\lambda$ and $\Delta\phi/180°$ are relative errors in estimated period, wavelength and propagation direction, respectively.

d_{Z-F} (km)	T_s (min)	ϕ (°)	T_e (s)	$\Delta T/T$	λ_e (km)	$\Delta\lambda/\lambda$	ϕ_e (°)	$\Delta\phi/180°$
3.0	4	300	720	-4.0%	10	-64%	280	-11%
3.0	1	300	762	1.6%	11	-61%	279	-12%
1.5	4	300	720	-4.0%	24	-14%	29	49%
1.5	1	300	756	0.8%	26	-7%	293	-4%
3.0	4	320	720	-4.0%	8	-71%	125	-97%
1.5	4	320	720	-4.0%	7	-75%	359	-33%

5 Discussion

This section discusses the results from the previous section, and also some observations made while developing the preprocessing and analysis methods described in Section 3.

5.1 Detection criteria and conditions on wave parameters

The greatest challenge to the comparison between all-sky imagers and three-field photometers was the low sampling frequency of the available data. The upper bound for the ratio between the frequency of the wave and the sampling frequency was set to 1/4 to avoid unreliable results close to the Nyquist frequency. The fact that the bound had to be lowered to allow detection

of waves forming part of the comparison basis, makes the validity of the comparison (Section 5.2.2) questionable.

Atmospheric gravity waves can't oscillate faster than the Brunt-Väisälä frequency, which is about $1/(5\text{ min}) = 0.0033$ Hz at the altitude of the OH airglow layer [Nakamura et al., 1999]. If one wishes to be able to detect all gravity waves and still fulfill the $f/f_s < 1/4$ requirement, one should have a sampling frequency of at least 0.013 Hz, i.e. measure the intensity at least once every 75 seconds. Sampling every minute is entirely possible for imagers, and photometers can sample faster still (Personal communication, P. Espy, May 20, 2015). The only detectors that may have trouble sampling this often, are one-field photometers or telescopes that have to be rotated to focus on the next field.

There is also a lower bound to the frequency of the wave, but it is dependent on the length of time over which the wave is observed, and not the sampling frequency. If a wave is observed for less than twice it's estimated period, the estimate is considered too uncertain and the wave is discarded. This means that short-lived waves or waves that the analysis erroneously consider short-lived, may not be detected. One would imagine spectral analyses of all-sky images encounter the same problem. Event analyses, on the other hand, allow us to detect a wave and estimate the wavelengths and periods if no Fourier transform is involved. It can however be argued that an estimate based on so few observations is still likely to be uncertain.

As the waves given in Table 1 are an example of, the waves easiest to detect by visual inspection are short waves of high frequency (short period). If the wavelength is too long and/or the phase speed too slow, it is very difficult for the human eye to spot it. Moreover, both event analysis and spectral analysis are limited by the size of the image; the wave must be recognizable as a wave within a single image, which puts a limitation on the wavelength (Personal communication, P.Espy, June 3, 2015). The analysis method described in this thesis does not share this spatial coverage limitation, but the phase speed and/or observation time of long waves must be sufficiently large or they may fail to fulfill the lower bound on frequency.

While imagers have an upper bound on the wavelengths they can detect, a system of photometers has a lower bound. From the intensity measurements acquired by photometers, no wavelengths smaller than twice the (longest) field separation can be found. So in this work no wavelengths below 12 km were expected to be seen. Small gravity waves are indistinguishable from ripples that are generated in-situ and carry no momentum into the meso-

sphere, so depending on the field separation, information is not necessarily lost. Suzuki et al. [2007] excluded all waves with horizontal wavelengths below 20 km in their calculations of momentum flux carried by observed gravity waves.

Despite it's restrictions, the three-field analysis will typically detect more wave events than an event analysis. The range of wave parameters it can detect is larger and a computer is more meticulous and less errorprone than a human. It should be noted that some waves may be misinterpreted as two waves if, in two different iterations of the analysis routine, they are estimated with periods which are too different for the program to recognize as equal. This problem could be effectively allivated by an increased sampling frequency, as this would improve the accuracy of the period estimates (Section 5.3).

5.2 Comments on detected waves and estimated wave parameters

Many waves were detected, and their wave parameters derived with the analysis method presented in Section 3.2. However, this is no proof that these waves were, in fact, real atmospheric gravity waves passing through the airglow layer. Visual detection of some of the shortest waves were attempted, without success. In order to judge if the estimated wave parameters (obtained with standard settings in the analysis) are reasonable, they are compared to wave parameters derived in a three-field photometer study. More importantly, the results of the search for the waves observed by Nærø [2013] are discussed.

5.2.1 Comparison with climatology from three-field photometer study of OH airglow

Despite the low sampling frequency, it would be interesting to compare the distributions of the wave parameters from the detected waves (Figure 12) to another climatology. Reid and Woithe [2005] used a three-field photometer to study airglow emissions from both OI and OH molecules, and from the OH airglow they detected 190 waves. They had a field separation of 13 km at the height of the OH layer. Their distributions of the horizontal wave parameter estimates have the following characteristics: they found periods in the range 0-200 minutes, and most were below 50 minutes (3000 seconds); they found

phase speeds in the range 0-300 m/s that were fairly evenly distributed; and they found wavelengths in the range of 50-400 km, and most of them were between 50-160 km.

This thesis' distribution of period estimates (Figure 12a) closely resembles the one presented in Reid and Woithe [2005]. The range of phase speeds found was slightly higher (Figure 12e), and the shape of the distribution resembles the one derived from an imager in Medeiros et al. [2003], but Reid and Woithe [2005] expressed surprise at the many high-speed waves in their distribution.

The greatest difference between the wave parameter estimates are found in the wavelength distributions. The range of wavelengths estimated in this work (Figure 12c) is much greater than the one in Reid and Woithe [2005]. Since atmospheric gravity waves have wavelengths up to a few hundred kilometers [Espy et al., 2006], the 1000-2000 km waves found in this work could be some other kind of wave perturbing the airglow, or, more likely, their wavelengths are overestimated. It is possible that the field separation is too small for long waves, introducing an error in the phase difference that is passed on to the estimate of the wavelength (and propagation direction). The cause of the lower bound to the wavelength estimate (Figure 12d) was explained in the previous section. Reid and Woithe [2005] expected no wavelengths below 26 km and were a bit surprised when none under 50 km were found.

A significant portion of the estimated propagation directions (Figure 12f) are the same as the direction of the z-axis for the chosen field configuration (300° relative to north). There seems to be a bias for this angle in the analysis procedure that should have been detected earlier and adressed.

All in all, the period distribution exhibits the best fit with the observations of Reid and Woithe [2005], strengthening the impression that the period estimates are the most accurate.

5.2.2 Comparison with wave parameters estimated by event analysis

The results of the search for the waves observed by Nærø [2013] are presented in Table 2. Judging by the relatively good period estimates (considering the low sampling frequency and the proximity of those waves to the Nyquist frequency) some of Nærø's waves were probably re-discovered by this work's analysis method. The estimated wavelengths, however, are both unlikely and in poor agreement with Nærø's. No information about the propagation

direction was collected for Nærø's waves, but since both the estimate of the wavelength and the estimate of the propagation direction rely on the phase difference, they are likely to be correlated.

This is not proof that the analysis method is working. However, some of the waves that should be the most difficult to reliably detect with this method, seems to have been, indeed, detected. It doesn't seem unreasonable to think that at least a good portion of the 36 wave events detected with standard settings, correspond to real waves, even though the derived wave parameter estimates may not be entirely accurate.

There is, of course, no guarantee that the wave parameters derived from the imager data with event analysis are any more accurate. The two methods have their own strengths and weaknesses. When visually detecting a very short, fast wave, misinterpretation of the direction of the wave by 180° would be a quite likely occurrence. This would not affect the estimate of the wavelength, but would result in inaccurate estimates of the period, phase speed and propagation direction (an 180° error). By comparison, the three-field analysis gives quite accurate period estimates (when the sampling frequency is sufficiently high), but gives more uncertain estimates of wavelength, phase speed and propagation direction.

The preference of imagers over three-field photometers in the geophysical research community may be partially explained by the consensus that short-period gravity waves carry most momentum [Matsuda et al., 2014], and the fact that imagers are well-suited for observing short-period waves. Does this mean, however, that the effect of the longer period gravity waves should be ignored? With high enough sampling frequency and a suitably chosen field configuration (see next section), photometer-systems should be able to reliably detect both low and high frequency waves. An alternative is also to choose a few select fields in the images and analyse them, as was done in this work. The benefit from this would be that a greater range of wave parameters could be obtained from the same images, and one could freely choose how many fields to integrate over.

5.3 Comments on the results from the simulated data

The first test with the simulated wave showed that the period estimate was improved by the reduction in wavefield complexity. While this was an expected result, the lack of change in the accuracy of the wavelength estimate was surprising. This suggests that something else, like the choice field con-

figuration, is of greater importance when determining the phase difference of the wave between the fields. A smaller error in the phase difference, gives smaller errors in both wavelength and propagation direction estimates.

Unsurprisingly, an increased sampling frequency improved the period estimates. The effect on the wavelength and propagation direction estimates seems to depend on the choice of field configuration again.

Since the simulated wave is fairly short, the wave parameter estimates were expected to improve if the field separation was reduced. For waves with propagation directions orthogonal to a line between two of the fields (here: $\phi = 300°$), this held true. The estimates of the wavelength, and possibly propagation direction, were greatly improved. However, the effect was lost for waves not orthogonal to any of the field pairs. Evidently, the quality of the wavelength and propagation direction estimates depends greatly on the field configuration.

While this shows how difficult it can be to choose an appropriate field configuration to facilitate observation of a wide range of different waves, it also suggests that a configuration of more than three fields would improve the overall accuracy of the wave parameter estimates. For a three-field system there are six favorable propagation directions for the wave parameter estimates. For a four-field system with no parallel fields, this is increased to twelve.

Increasing the number of fields will of course introduce other issues, depending on the observation system used to acquire the data. A four-field photometer is more expensive than a three-field photometer, and the computation time of the analysis will increase. But the most important thing to consider, is the change in sampling frequency if the observation system can't sample at the fields simultaneously. As experienced in the author's specialization project, the sampling frequency for a telescope that has to rotate between fields, easily becomes so low that one would expect to obtain better results with three fields than with four.

6 Conclusion

Small-field observation systems detect atmospheric gravity waves over a wide range of wave parameters. Unlike imagers, the wave parameters are inferred in the time series and are therefore not limited by the finite field of view of the imager. Thus, these systems are able to capture waves with wavelengths

much larger than the imager field of view and correspondingly longer periods. However this time-domain analysis is more limited by the sampling frequency than imaging systems for the short period waves that typically have shorter (<100 km) wavelengths. The data analysed in this work showed that with the low sample frequency used by the imager, there was a limited sample of waves that could be compared using the two techniques. That is, the small-field observations favoured long period and wavelength waves, while the imager analysis was better suited to shorter period and wavelength waves. However, some of the waves detected by event analysis seemed to correspond to those detected by the small-field analysis, even though the wavelength comparison exceeded the uncertainties.

The three-field analysis developed and utilized in this work returns very accurate period estimates that corresponded to the waves observed in the image analysis. However, the shortest periods that could be derived using this technique were limited by the sampling frequency of the imager. The estimates for the wavelength and propagation in this technique depend heavily on the field configuration, but generally the wavelengths have higher uncertainties than the period. Thus there was substantial disagreement between the wavelengths observed at a given period between the two techniques. In future work, it may be possible to optimize the sampling field and sampling frequency so that there is a one-to-one correspondence between the two techniques for waves <100 km.

In summary, event analyses are well suited for deriving the wavelength of short-period waves, but the periods are more uncertain. In addition, the maximum wavelengths and periods are limited by the field of view of the imager. Conversely, small-field analyses are able to derive the periods with low uncertainty, but are limited to frequencies well below the Nyquist sampling frequency. Thus, with the non-optimized sampling periods and sampling spacing used, there was substantial disagreement between the derived wavelengths for the narrow range of short wavelengths and periods for which the two techniques overlapped. With further optimization, the analysis developed in this work demonstrates that the utilization of small-field observation systems like photometer-systems or astronomical telescopes has great potential to supplement and extend imager observations.

References

David G. Andrews. *An Introduction to Atmospheric Physics*. Cambridge University Press, 2nd edition, 2010.

D. J. Baker and A. T. Stair. Rocket Measurements of the Altitude Distributions of the Hydroxyl Airglow. *Physica Scripta*, 37, 1988.

P. J. Espy, R. E. Hibbins, G. R. Swenson, J. Tang, M. J. Taylor, D. M. Riggin, and D. C. Fritts. Regional variations of mesospheric gravity-wave momentum flux over Antarctica. *Annales Geophysicae*, 24, 2006.

Morten Hatlen. On-board, Fourier-Based Image-Analysis System for Satellite Observation of Gravity Waves. Master's thesis, Norwegian University of Science and Technology, 2013.

Endre Asheim Hennum. A new algorithm for remote sensing mesopause temperatures using the hydroxyl airglow. Master's thesis, Norwegian University of Science and Technology, 2013.

J. S. Kennedy. Comments on 'On Detrending and Smoothing Random Data' by A. J. Owens. *Journal of Geophysical Research*, 85, 1980.

Darin C. Koblick. SolarAzEl.m: Solar azimuth and elevation, computer software, 2009.

T. S. Matsuda, T. Nakamura, M. K. Ejiri, M. Tsutsumi, and K. Shiokawa. New statistical analysis of the horizontal phase velocity distribution of gravity waves observed by airglow imaging. *Journal of Geophysical Research: Atmospheres*, 119, 2014.

A.F. Medeiros, M.J. Taylor, H. Takahashi, P.P Batista, and D. Gobbi. An investigation of gravity wave activity in the low-latitude upper mesosphere: Propagation direction and wind filtering. *Journal of Geophysical Research*, 108, 2003.

Karoline Nærø. Gravity Wave Refraction in the Atmosphere: Ray tracing versus Geometric Location from a Single Image. Master's thesis, Norwegian University of Science and Technology, 2013.

T. Nakamura, A. Higashikawa, T. Tsud, and Y. Matsushita. Seasonal variations of gravity wave structures in OH airglow with a CCD imager at Shigaraki. *Earth Planets Space*, 51, 1999.

Dep.OfPhysics NTNU. Data acquired with an Andor spectrometer at Dragvoll, Trondheim.

I. M. Reid and J. M. Woithe. Three-field photometer observations of short-period gravity wave intrinsic parameters in the 80 to 100 km height region. *Journal of Geophysical Research*, 110, 2005.

S. Suzuki, K. Shiokawa, Y. Otsuka, T. Ogawa, M. Kubota, M. Tsutsumi, T. Nakamura, and D. C. Fritts. Gravity wave momentum flux in the upper mesosphere derived from OH airglow imaging measurements. *Earth Planets Space*, 59, 2007.

C. Torrence and G. Compo. Wavelet Software.

C. Torrence and G. Compo. A Practical Guide to Wavelet Analysis. *Bulletin of the American Meteorological Society*, 79, 1998.

Jonathan Woithe. *Optical Stuides of the Mesospheric Region*. PhD thesis, University of Adelaide, 2000.